Journal of Applied Fluid Mechanics, Vol. 18, No. 11, pp. 2893-2912, 2025.
Available online at www.jafmonline.net, ISSN 1735-3572, EISSN 1735-3645.
https://doi.org/10.47176/jafm.18.11.3424

Pressure Pulsation Characteristics and Flow-induced Vibration Optimization in a Turbine Runner under Low Flow Conditions

H. Song[1†], W. Xie[1], W. Han[1], H. Qiu[2], Z. Guan[3], S. Wang[4] and X. Huang[4]

[1] *College of Energy and Power Engineering, Lanzhou University of Technology, Lanzhou, Gansu, China*
[2] *Electrical and Information Engineering Institute, Zhengzhou University of Light Industry, Zhengzhou, Henan, China*
[3] *Power Generation Operations Department, Gansu Chaijiaxia Hydropower Co Ltd, Lanzhou, Gansu, China*
[4] *College of Electrical and Information Engineering, Lanzhou University of Technology, Lanzhou, Gansu, China*

†*Corresponding Author Email: songhb@lut.edu.cn*

ABSTRACT

Hydropower systems, as core components for electricity regulation in renewable energy infrastructures, are increasingly operating under off-design conditions, such as high- and low-flow scenarios. Pressure pulsations induced by off-design operation have posed severe threats to the stability and reliability of flow-passing components. In this study, a 24 MW bulb turbine was selected as the research object. A transient fluid-structure interaction (FSI) method based on the finite element method (FEM) and finite volume method (FVM) was employed to investigate pressure variations and abnormal pulsations within the runner region. The reliability of the flow field analysis was validated through experimental data. The structural response of flow-passing components under complex pressure distributions was evaluated, and a multi-parameter collaborative optimization model was developed. An improved structural design was proposed to mitigate pressure pulsations under off-design conditions. Results show that, under flow-induced pressure mapping, the optimized structure achieved an average increase of 4.04% in prestressed modal frequency and 58.45% in wet modal frequency compared to the original structure, along with a significant alleviation of stress concentration phenomena. This study provides valuable insights into enhancing the safe operation of hydraulic turbines within multi-energy complementary renewable energy systems.

Article History

Received February 11, 2025
Revised June 5, 2025
Accepted June 8, 2025
Available online September 3, 2025

Keywords:

Pressure pulsation
Flow-induced vibration
Hydraulic turbine
Computational fluid dynamics
Fluid-structure interaction

1. INTRODUCTION

Circumferentially stiffened cylindrical shells are widely used in various underwater structures, including subsea pipelines (Wang et al., 2023), military submarines, sightseeing submersibles (Yang et al., 2021) and turbines. During operation, these shells are subjected to combined loads such as hydrostatic pressure, hydraulic impacts, and self-weight, leading to issues such as fatigue, vibration, and even fractures. Turbines are typical underwater engineering structures, and their operational stability is crucial for industrial and daily activities. The runner chamber, which is an essential flow-through component of turbines, also represents a typical stiffened structure. Over time, it becomes prone to structural fatigue, vibration, and wear owing to continuous hydraulic impacts, which ultimately affect the lifespan of the unit. Consequently, the structural strength and vibration characteristics of the runner chamber during turbine operation have become key research topics.

The stability of underwater structures is fundamentally affected by the internal flow characteristics of the flow field. A comprehensive understanding of the complex dynamic behavior of the flow field is essential to accurately evaluate the vibration characteristics and structural reliability of these structures throughout their operational lifespan. Computational fluid dynamics (CFD) has emerged as a powerful tool for predicting internal flow characteristics (Ahn et al., 2017, 2020) , with advancements in flow field models and numerical methods (Guo et al., 2015) further enhancing computational accuracy. In axial-flow fluid machinery, such as bulb turbines, complex flow phenomena like vortex shedding and vortex rope formation (Roig et al., 2022) under off-design conditions can generate high-amplitude pressure pulsations, leading to significant damage to flow components. Moreover, operational factors such as load variations (Amiri et al., 2016; Soltani Dehkharqani et al., 2019), head fluctuations (Zhao et al., 2023), and cavitation (Li et al., 2023) can exacerbate

vibration and noise issues in these components. To address these challenges, fluid-structure interaction (FSI) algorithms have been widely employed to study the coupling between fluid and solid components, demonstrating excellent agreement between numerical simulations and experimental data across various turbine types (Zhang et al., 2019; Georgievskaia, 2021; Cao et al., 2022a, b; Moraga et al., 2024). Although existing research has extensively investigated the impact of fluid forces on impeller components, including modal analyses and wear mechanisms, studies focusing on the runner chamber which is a critical flow-through component remain limited highlighting a significant gap in the current literature.

Theoretical studies of cylindrical shells have attracted the interest of several researchers. Lee and Kwak (2015) established a dynamic model of free vibration for cylindrical shells using the Rayleigh-Ritz method, derived explicit expressions for the mass and stiffness matrices of the structure, and compared the accuracy of the natural frequencies calculated using Sander's, Love's thin-shell, Reissner's, Flugge's, and Vlasov theories. Liu et al. (2022) developed an equivalent orthotropic shell model using homogenization techniques, combining Love's thin-shell theory and obtaining the natural frequencies and forced vibration responses using a modified Fourier series and the Rayleigh-Ritz method. Chen et al. (2015) investigated the free and forced vibration characteristics of ring-stiffened conical-cylindrical composite shells using substructure division and multiple function descriptions of motion. Gao et al., (2024) developed an analytical model of the vibroacoustic response of ring-stiffened cylindrical shells, studying the effects of load parameters, boundary constraints, and structural parameters on the acoustic-vibration response, providing valuable references for ring-stiffened structure design. Considering the influence of boundary constraints, Su et al. (2014) used variational principles and the modified Fourier series to accurately analyze the vibration characteristics of cylindrical shells under arbitrary boundary conditions. Building on these theoretical advancements, numerical studies of ring-stiffened structures are abundant. Esmaeilzadehazimi et al. (2024) used a hybrid finite element method to simulate and analyze fluid-filled ring-stiffened conical shells to verify their reliability through experiments and provide a new option for numerical calculations. Jin et al. (2021) developed a constraint shell finite element method (cFEM) to analyze the elastic buckling behavior of thin-walled sections under bending. The cFEM method implemented in ANSYS demonstrated its potential for structural analysis and design. Chen et al. (2024) combined numerical simulations and water tank tests to study the heat transfer characteristics of ring-stiffened tanks and the flow characteristics of internal flow channels. Shan et al. (2024) used numerical analysis to investigate the stability of corrugated cylindrical shells under uniform or concentrated pressure. Bai et al. (2019) focused on thin-walled cylindrical shells with initial geometric imperfections, discussing the mechanism of influence of geometric defects on shell stiffness and stability based on the Reduction Stiffness Method (RSM).

The response surface methodology is an optimization technique that constructs mathematical models based on experimental data or numerical simulation results. By systematically analyzing multiple variables, the optimal combination of design parameters was identified. In the structural optimization of hydraulic machinery, RSM has been widely used as an effective tool for optimizing fluid-structure interactions. In recent years, RSM has been successfully applied to the optimization of hydraulic vortex turbines, helping researchers determine the key geometric parameters that influence water flow circulation, thereby improving turbine efficiency (Velásquez et al., 2022). Additionally, RSM is often combined with optimization techniques such as genetic algorithms (GA) to optimize the flow passage structures of wind turbines, significantly enhancing their power coefficients (Rahmatian et al., 2023). Another study applied RSM to optimize the design parameters of turbine runners, including the number of blades, their positioning, and the ratio of the blade diameter to the flow passage diameter, effectively improving the overall turbine performance (Velasquez et al., 2024). However, most RSM studies have relied on traditional Monte Carlo sampling or factorial design methods, which have limited sample points and insufficient global coverage. By contrast, Latin Hypercube Sampling (LHS) ensures a more uniform distribution across all dimensions through stratified sampling, leading to more evenly distributed samples and more reasonable optimization results. Thus, the LHS is a superior approach for optimizing the design of hydraulic machinery.

Despite the significant progress in studying the vibration characteristics and optimizing ring-stiffened structures, research on the long-term stability and fatigue behavior of large-scale ring-stiffened structures remains limited, particularly under complex flow field conditions. As a typical ring-stiffened structure, the runner chamber in turbine units is particularly susceptible to fatigue damage, stress concentration, and vibration owing to the combined effects of fluctuating fluid impact loads and prolonged hydrostatic pressure. This research gap underscores the need for a comprehensive study of the vibration characteristics of the runner chamber under such complex conditions, which are critical for enhancing the turbine unit stability and extending the service life. This study addresses this gap by investigating the vibration response and optimizing the runner chamber in a bulb turbine through a fluid-structure interaction (FSI) analysis. The fluid-structure interaction model is specifically chosen for its ability to accurately capture the complex coupling between flow-induced pressure fluctuations and structural vibration, which is a critical factor in understanding and mitigating fatigue damage. By incorporating both the pressure pulsation distribution in the runner region and the structural vibration characteristics, this approach offers a higher degree of precision than traditional methods. First, a numerical model of the internal flow field is established and validated experimentally, followed by the development of a mathematical model of the runner chamber using

Table 1 Hydraulic turbine design parameters

Parameter name	Parameter value	Parameter name	Parameter value
Type of turbine	GZ995-WP-720	Rated speed	68.18 r/min
Rated capacity	24.65 MW	Rated flow	399.2 m³/s
Maximum head	10 m	Minimum head	3.1 m
Rated head	6.8 m	Draft head	-8.8 m
Installation elevation	1532.2 m	Number of runner blades	4
Number of guide vanes	16	Diameter of runner	7.2m

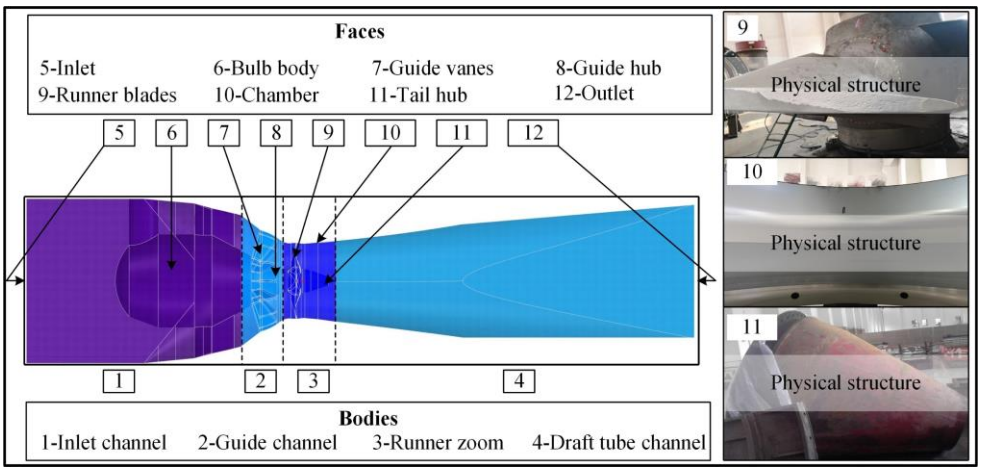

Fig. 1 Schematic structure of the hydraulic turbine computational domain

Flügge's thin-shell theory to analyze stress-strain relationships. The modal expansion method is then applied to investigate the vibration frequencies and modes under fluid loading and structural constraints. Finally, optimization methods based on experimental design techniques are employed to identify the optimal structural configuration, and the feasibility of the optimized design is validated through both simulations and experiments. The results provide valuable insights for improving the long-term stability and reliability of large-scale ring-stiffened structures, contributing to their engineering applications in turbine units.

2. PHYSICAL FLOW MODEL AND NUMERICAL CALCULATION METHODS

2.1 Geometric Modeling

This study focused on a 24 MW bulb turbine generator with the relevant design parameters listed in Table 1. The computational and surface domains of the turbine were constructed based on the design parameters of the hydropower station and the turbine, as shown in Fig. 1. The computational domain encompasses the inlet flow passage, guide vane flow passage, runner chamber, and tailwater flow passage, whereas the surface domain is used to set the boundary conditions and viewing results.

In studies on bulb turbines, water is typically considered an incompressible fluid. As water experiences minimal heat exchange during its flow as a medium, energy conservation can be neglected. Based on this assumption, the continuity equation and the momentum conservation equation are employed to describe the complex three-dimensional incompressible viscous flow within the flow passage (Weili et al., 2012).

$$\begin{cases} \dfrac{\partial \rho}{\partial t} + div(\rho \boldsymbol{u}) = 0 \\ \dfrac{\partial(\rho u)}{\partial t} + div(\rho u \boldsymbol{u}) = div(\phi gradu) - \dfrac{\partial P}{\partial x} + S_u \\ \dfrac{\partial(\rho v)}{\partial t} + div(\rho \boldsymbol{u} v) = div(\phi gradv) - \dfrac{\partial P}{\partial y} + S_v \\ \dfrac{\partial(\rho w)}{\partial t} + div(\rho \boldsymbol{u} w) = div(\phi gradw) - \dfrac{\partial P}{\partial z} + S_w \end{cases} \tag{1}$$

In the above equation, ρ represents fluid density; u, v and w are the velocity components in the x, y and z directions, respectively; P represents pressure; S_u, S_v and S_w are the generalized source terms for momentum conservation in the respective directions. Given the complex curved surfaces of the guide vanes, impeller, and runner chamber walls, and the need to capture the overall flow characteristics, this study employed the SST $k-\varepsilon$ turbulence model.

The simulations were conducted using the finite volume method (FVM) implemented in ANSYS Fluent. To improve the accuracy of the solution while maintaining numerical stability, the second-order upwind scheme was applied for spatial discretization of both the momentum and turbulence equations. Temporal discretization was performed using a second-order implicit scheme, which enables stable and accurate resolution of transient flow behavior with relatively large time steps. Pressure-velocity coupling was handled using the PISO (Pressure-Implicit with Splitting of Operators) algorithm, which is well-suited for unsteady flow simulations due to its enhanced convergence characteristics. Gradient terms

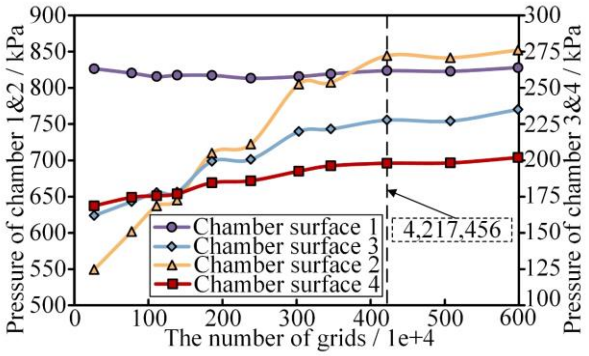

(a) Effect of the number of grid cells on the results of pressure calculations

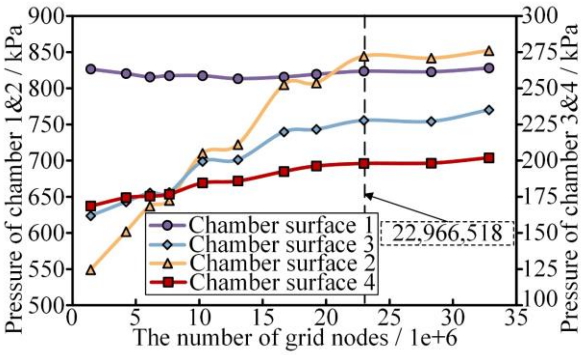

(b) Effect of the number of mesh nodes on the results of pressure calculations

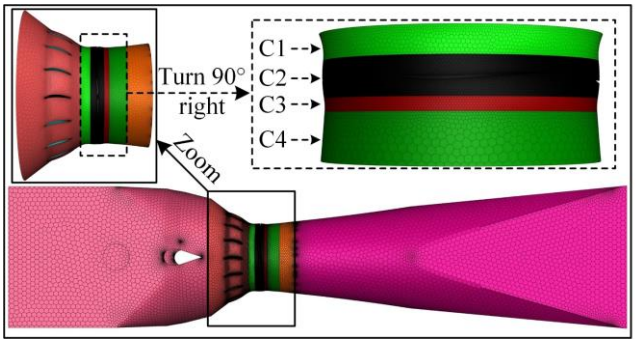

(c) Watershed grid display

Grid parameters	
Total units	4217456
Total nodes	22966518
Skewness	0.19981
Aspect ratio	1.7659
y+	5
Element quality	0.85738

(d) Grid parameters

Fig. 2 Effect of mesh resolution on calculation results

were evaluated using the least-squares cell-based method to ensure accurate interpolation on unstructured meshes. These settings collectively ensure that the numerical scheme is consistent with the conservation principles of FVM, and capable of capturing the complex, vortex-dominated, transient flow within the bulb turbine.

Considering the complex geometry of the guide vanes, impeller, and runner chamber walls, along with the necessity to accurately capture flow characteristics, this study used the ANSYS Fluent software and the SST k-ε turbulence model. This model integrates the benefits of both the standard k-ε and k-ω models. It employs the k-ω model in the near-wall regions to better simulate shear flow behavior near the surfaces, while applying the k-ε model in the free-stream regions to enhance the prediction accuracy of the overall flow. The parameters of the turbulence model, specifically Cμ, C1-ε, and C2-ε, were set to 0.0845, 1.42, and 1.68, respectively, to optimize both the accuracy and stability of the flow field results. To further improve the simulation, the differential viscosity model and swirl-dominated flow option were activated to address potential large-scale vortex formation. These settings yielded highly accurate results for capturing the critical flow features of a bulb turbine under low-flow conditions.

For the transient flow field calculations, the time step was set to 0.0024 s, corresponding to a 1° rotation of the runner, and the results were saved every 10° of rotation. This time step ensures a good balance between computational efficiency and the accurate capture of transient flow dynamics. This approach enabled a detailed examination of the flow behavior within the bulb turbine during low-flow scenarios while maintaining the stability of the simulations.

To validate the influence of the mesh resolution on the computational results, the runner chamber surface domain was divided into four regions (C1, C2, C3, and C4) along the axial direction, from the upstream to the downstream side, and the wall pressure was evaluated under steady-state conditions, as shown in Fig. 2(a) and (b). When the number of mesh elements in the computational domain reached 4,217,456 and the number of mesh nodes reached 22,966,518, the wall pressure curves stabilized. Considering both computational efficiency and accuracy, a mesh configuration with 4,217,456 elements was selected for subsequent numerical calculations, as shown in Fig. 2 (c). Figure 2 (d) presents detailed grid parameters. The average mesh element quality was 0.85738, with a skewness of 0.19981, and an aspect ratio of 1.7659, indicating a well-conditioned mesh suitable for accurate numerical simulations. Additionally, the non-dimensional wall distance (y^+) was evaluated and found to be approximately 5, which is within an acceptable range for the turbulence model employed, ensuring the proper resolution of near-wall flow structures.

2.2 Pressure Pulsation Distribution Characteristics in the Runner Chamber

In this study, the analysis of the flow field pressure distribution focuses on the flow characteristics within the runner section. Since the flow pattern in the runner section exhibits a largely symmetrical behavior during blade

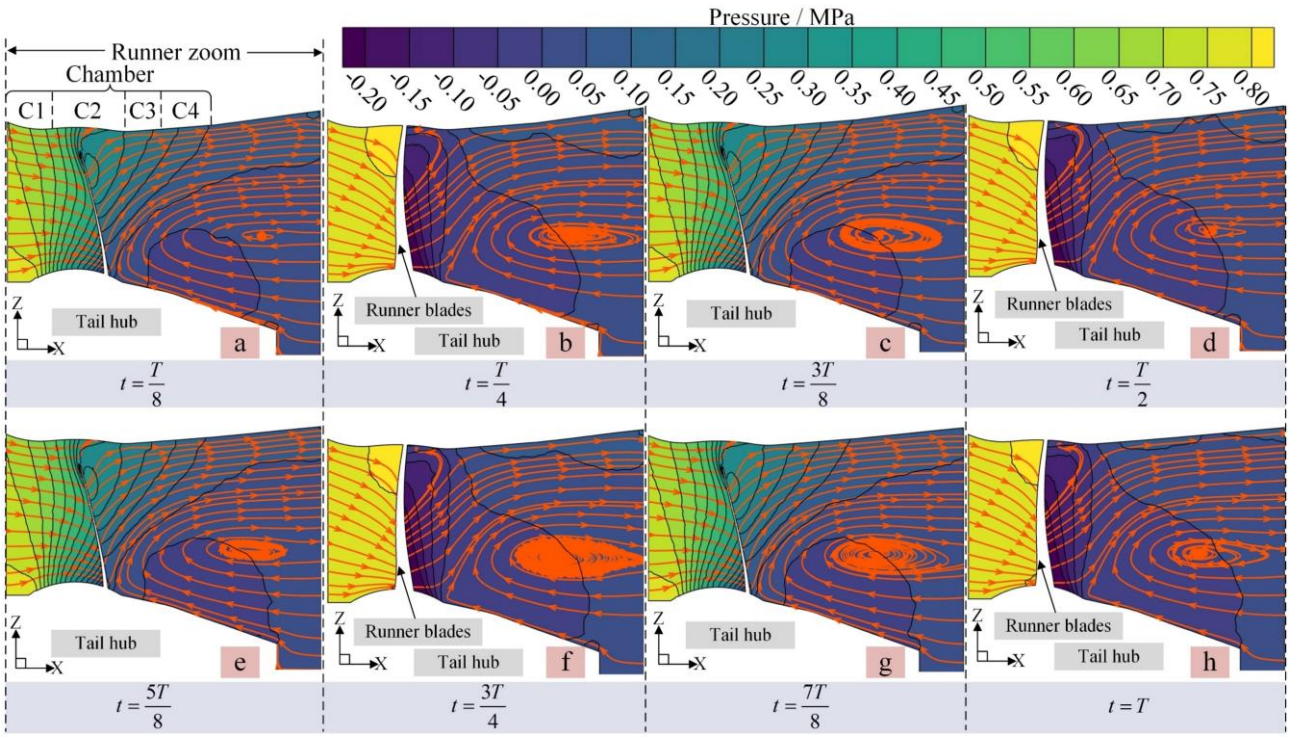

Fig. 3 Pressure and streamline distribution in the runner area

rotation, the upper half of the runner section's cross-section was selected for detailed observation of pressure and flow trajectory distribution at different time steps, as shown in Fig. 3.

The analysis reveals that the guide vanes play a significant role in streamlining the flow, resulting in a distinct high-pressure zone on the upstream side of the runner section. Under the influence of centrifugal force, the fluid flows axially while gradually converging toward the central axis as the blades rotate, without forming any noticeable vortices. At times when the blade is not passing through (e.g., a, c, e and g), the pressure gradient on the downstream side changes slowly, and the flow region near the runner chamber walls exhibits a uniform flow pattern, indicating a stable flow field. However, when the blade passes through (e.g., b, d, f and h), significant pressure differences appear on both sides of the blade. Additionally, the influence of the expanding tailwater pipe wall leads to a reverse pressure gradient in the downstream flow, which disturbs the flow characteristics.

Moreover, by examining the flow direction on the downstream side, two distinct flow patterns can be identified. First, the fluid near the runner chamber wall flows uniformly in the axial direction, entering the tailwater pipe. Second, the fluid near the tailwater cone is influenced by the rotating components, forming distinct recirculating vortices. These vortices arise primarily due to the centrifugal force generated by the rotating components and the inertia of the fluid, resulting in localized backflow and disturbances in the flow.

The distribution characteristics of the pressure gradient are utilized to further reveal the relationship between fluid flow behavior and the loading characteristics at the fluid-structure interface. As a fundamental concept in fluid mechanics, the pressure gradient is closely related to flow characteristics, energy transformation within the flow field, and fluid dynamic behavior. It is defined as the pressure variation per unit distance in space, typically expressed as $\Delta P/\Delta x$, where P denotes the pressure and x represents the spatial coordinate along the direction of fluid motion. The magnitude of the pressure gradient reflects the intensity of pressure variation in a local region: a larger gradient indicates a more abrupt pressure change, whereas a smaller gradient suggests a more gradual variation.

Figure 4 presents the distribution of the pressure gradient at the fluid-structure interface within the runner region at different time instants over one complete rotation cycle. It can be observed that, under the action of impeller rotation, the pressure gradient at the interface exhibits a periodic and cyclic pattern. The peak values of the pressure gradient are primarily concentrated at the leading and trailing edges of the blades, indicating that these areas experience significant pressure variations during the flow process. Along the mainstream flow direction, the pressure gradient is more pronounced at the leading edge (the upstream-facing side) of the blade, implying that the pressure changes are most intense in this region. In contrast, the remaining areas of the interface, aside from the blades, exhibit relatively gentle pressure variations, suggesting a more stable flow behavior.

Moreover, particular attention must be paid to the pressure pulsations occurring on the wall surfaces corresponding to the impeller position. Due to rapid local pressure fluctuations induced by impeller rotation, the wall regions may experience significant periodic pulsation phenomena, which can have a substantial impact on the flow-induced vibration characteristics and fatigue

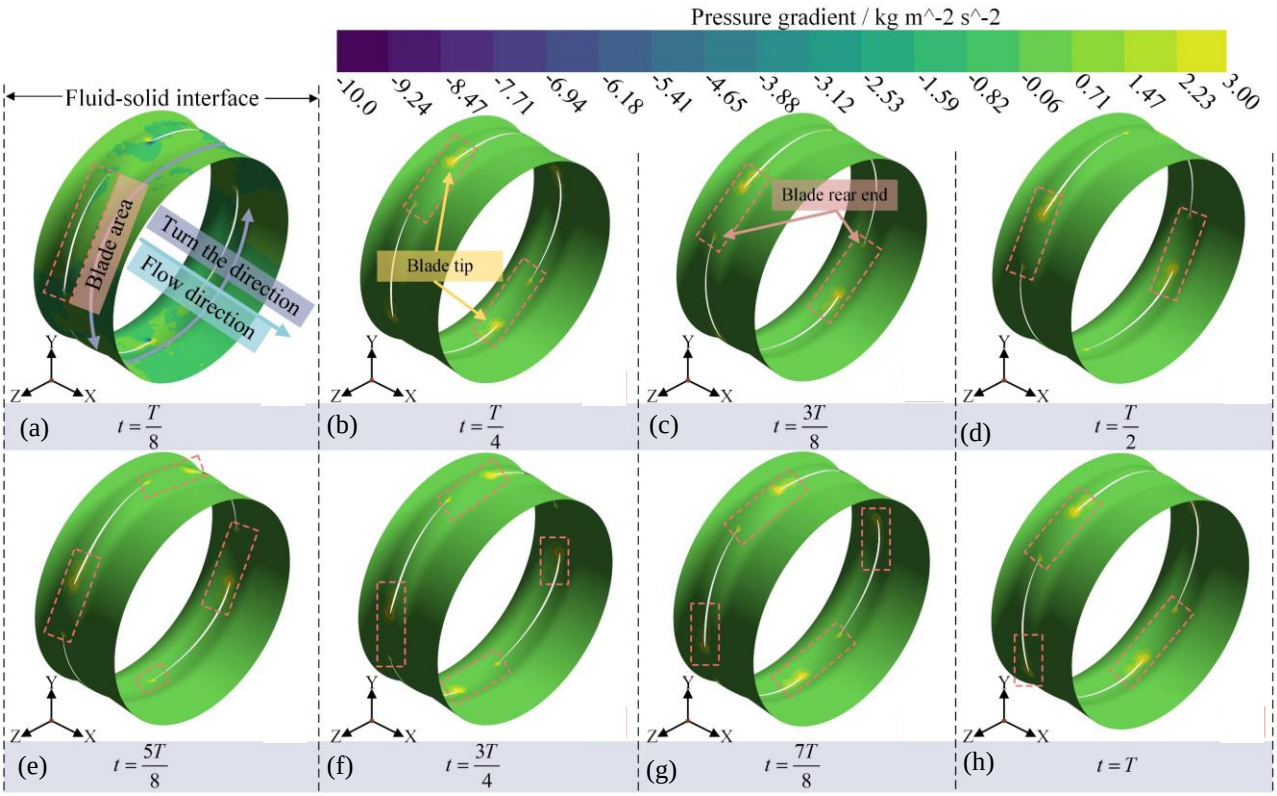

Fig. 4 Display of the pressure gradient in the runner area

performance of the structure. Therefore, understanding the spatial and temporal evolution of the pressure gradient at the fluid-structure interface is critical for accurately capturing the fluid-structure interaction dynamics.

As an axial fluid flow machine, a tubular water turbine experiences periodic variations in the internal flow field pressure, which directly affect the walls of the runner chamber, leading to vibrations and structural damage. The dynamic-static interference between the guide vanes and blades, interaction between the blades and chamber wall, and backflow effect of the tailwater pipe contribute to the significant differences in pressure pulsations across various regions of the flow passage. To analyze these differences in depth, a Fourier transform is applied to the time-domain pressure pulsation signals collected from each monitoring point, to extract their frequency-domain characteristics. The pressure pulsation coefficient is introduced to characterize the magnitude of the pressure pulsation relative to the pressure potential energy, as shown in Eq. (2).

$$C_p=\frac{\Delta p}{\rho g H_{rat}}\times 100\%=\frac{p-\bar{p}}{\rho g H_{rat}}\times 100\% \tag{2}$$

where Δp represents the absolute amplitude of the pressure pulsation, defined as the difference between the computed pressure p and average pressure $\bar{p}$, measured in Pa. $\rho$is the density of water and is taken as $1000\ \mathrm{kg/m^3}$. g is the acceleration due to gravity and is taken as $9.81\mathrm{m/s^2}$. Additionally, based on the definitions of rotational frequency and blade frequency in the literature, the turbine's rotational frequency is $f_s=n/60=1.1364\mathrm{Hz}$ and blade frequency is $f_b=Z_r\times f_s=4.5455\mathrm{Hz}$.

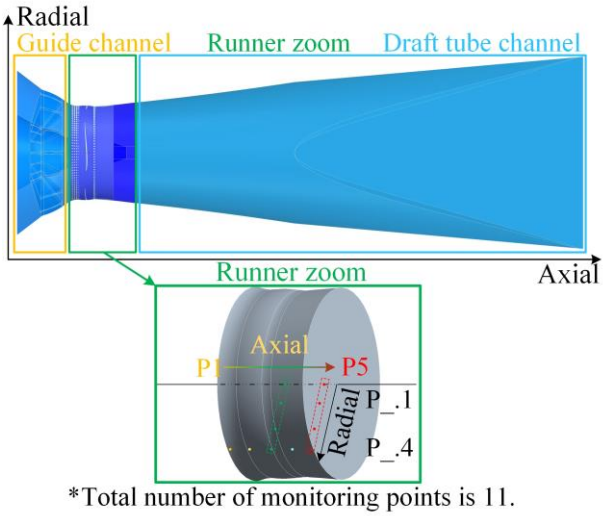

Fig. 5 Schematic representation of monitoring points in the computing domain

To obtain the distribution pattern of the pressure pulsations in the runner region of the turbine under low-flow conditions, monitoring points must be set along both the axial and radial directions within the runner chamber. According to Wu et al. (2021), pressure pulsations exhibit a periodically symmetrical distribution around the main shaft. Therefore, monitoring points are set along one side of the main shaft, as shown in Fig. 5. A total of 11

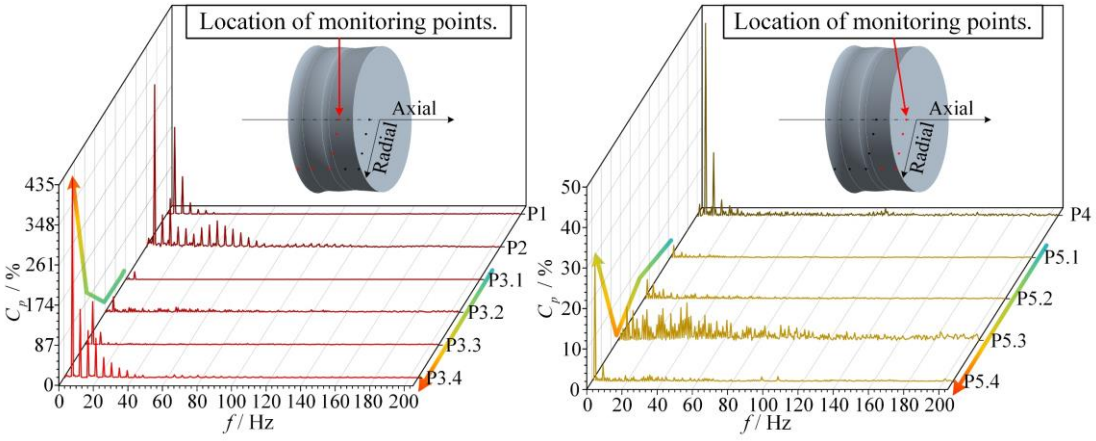

(a) Pressure pulsation spectrum from point P1 to P3.4.

(b) Pressure pulsation spectrum from point P4 to P5.4.

Fig. 6 Spectrogram of pressure pulsations at monitoring points

monitoring points is distributed uniformly along the axial direction in the runner area, organized into 5 groups, with 1 and 4 points radially distributed in each group, respectively.

The frequency spectra of the pressure pulsations at the monitoring points are shown in Fig. 6. The primary contributing frequencies of the pressure pulsations in the runner area are 4.54 Hz and 1.14 Hz, with higher harmonics of frequencies up to 200 Hz being present in the pulsation spectra near the wall and in the tailwater pipe region. At all the monitoring points, the pressure pulsation coefficient for the lower harmonics was the highest. The low-frequency component at 4.54 Hz is close to the blade frequency and the frequency of the maximum amplitude pulsation in the vibration tests, which agrees with the findings of Wang and Luo (2010). This indicates that the periodic hydraulic shock imposed cyclic loads on the runner chamber, resulting in severe vibrations. Furthermore, the analysis of the radial pressure pulsations revealed that the pressure pulsation coefficient gradually increased from the central axis toward the wall-monitoring points. The pressure pulsation coefficients at the central axis positions (P3.1, P5.1) are relatively low, whereas those closer to the wall (P1, P2, P3.4, P4, and P5.4) exhibit significantly higher values. The pressure pulsation coefficient at the P3.4 monitoring point, located immediately behind the impeller, reaches a maximum of 431.43%.

In addition, the pressure pulsations at the wall-monitoring points displayed a nonlinear distribution along the axial direction. Influenced by impeller rotation, the pressure pulsation coefficients at P1 and P2 gradually increased, peaking at P3.4. As the distance from the impeller region increases, the maximum amplitude of the pressure pulsations at the monitoring points consistently decreases, which is highly consistent with the conclusions of (Wu et al., 2021).

Statistical analyses were performed on the pressure pulsation frequency spectra at different monitoring points to extract the maximum pressure pulsation coefficients

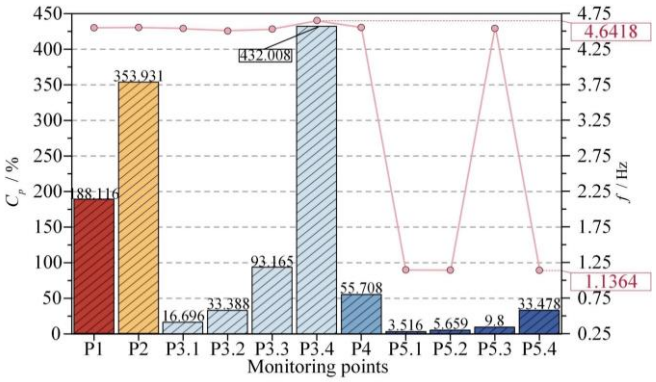

Fig. 7 Comparison of pressure pulsation amplitude and frequency

and their corresponding frequencies, as shown in Fig. 7. In the runner chamber impeller region (monitoring points P1–P3.4), the maximum frequencies of the pressure pulsation coefficients are primarily concentrated around the blade frequency (4.5455 Hz), indicating that the number of blades significantly influences the pressure pulsations within the runner chamber. In contrast, at the rear end of the runner zone, the maximum frequency is closer to the shaft frequency (1.1364 Hz), suggesting that this region is more susceptible to the influence of the rotational speed of the unit.

Under the influence of the impeller, the pressure pulsation coefficients at the monitoring points increased gradually in the radial direction, first increasing and then decreasing along the axial direction. A quantitative analysis of the amplitude variations at the axial wall-monitoring points revealed that the amplitude at monitoring point P2 in the impeller region increased by 88.15% compared to P1, and at the trailing edge of the impeller (monitoring point P3.4), the amplitude further increased by 22% compared to P2, reaching its maximum. Conversely, the amplitudes at monitoring points P4 and P5.4, which were farther from the impeller region,

Table 2 Runner chamber vibration test equipment

Name	Models	Measurement range	Measurement accuracy
Vibration Test Analyser	TTS332	±24V	Amplitude error＜0.5%
Low Frequency Velocity Transducer	MLS-9	0.5~200Hz	Sensitivity 8V/mm

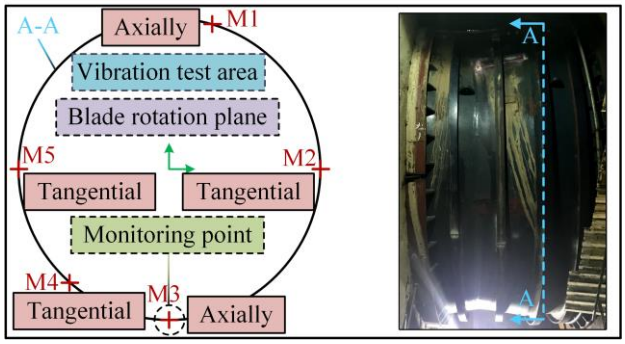

Fig. 8 Schematic diagram of experimental test location

gradually decreased with reductions of 87.11% and 39.9%, respectively.

Observing the amplitude variation trends at the radial monitoring points, the results at monitoring points P3.1–P3.4 in the impeller region indicate that the pressure pulsation variations near the central axis are relatively uniform. In contrast, significant jumps in the amplitudes of the pressure pulsation occurred at the wall-monitoring points, with the amplitude at P3.4, increasing by 363.38% compared with that at P3.3. For monitoring points P5.1–P5.4, which are farther from the impeller region, a similar jump occurs near the wall, with P5.4 increasing by 241.61% compared to P5.3; however, the overall amplitudes are lower.

To investigate the influence of pressure pulsations on the vibration of the runner chamber, a vibration test was conducted on a 16 MW turbine runner chamber under low-flow conditions, which closely resembled the conditions for the numerical calculation. The test equipment and parameters are listed in Table 2. An MLS-9 low-frequency velocity sensor was used to capture low-frequency vibration signals and effectively detect minute vibrations in the runner chamber. The TTS332 vibration testing analyzer, equipped with high-precision data acquisition and real-time spectrum analysis capabilities, is suitable for studying complex fluid vibration characteristics Fig. 8.

In the experiment, the MLS-9 low-frequency velocity sensors were arranged circumferentially on the working plane of the runner chamber blades, with five measurement points installed via magnetic bases. The vibration signals were collected and analyzed using a TTS332 vibration testing analyzer, and the vibration spectrum results are shown in Fig. 9.

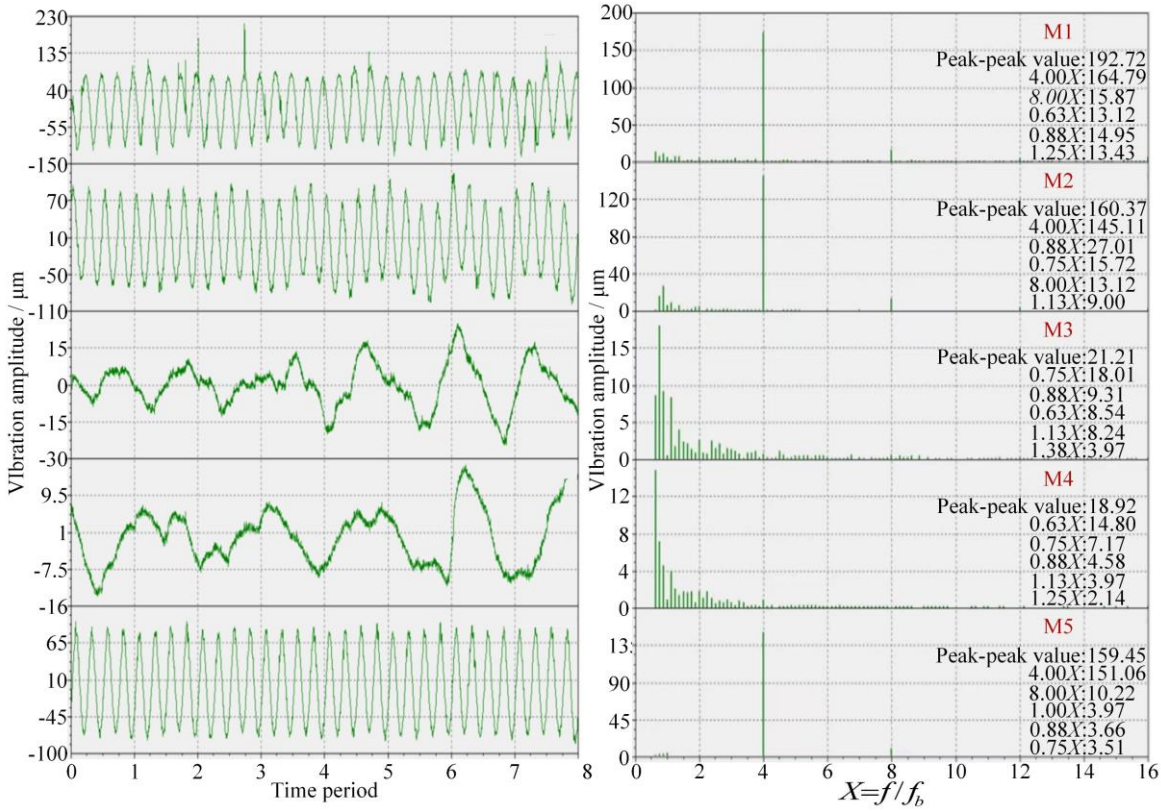

(a) Variable load 16 MW runner chamber vibration waveforms

(b) Variable load 16 MW runner chamber vibration spectrum

Fig. 9 Vibration test results

Table 3 Runner chamber material properties

Parts	Material	Mudulus of elasticity / MPa	Poissons ratio	Density / kg/m³	Yield strength / MPa	Tensile strength / MPa
Cylinder	0Cr13Ni5Mo	2.00e+05	0.284	7.96e+03	540	686
Reinforece stiffener	Q235	2.00e+05	0.284	7.85e+03	250	460

The experimental results indicated the following: (1) Under non-design conditions, the vibration spectra at all measurement points within the runner chamber contained varying degrees of higher harmonics, which were particularly pronounced near the bottom of the runner chamber. (2) At the upper measurement points, M1, M2, and M5, the pressure pulsation predominantly exhibited a frequency four times the shaft frequency, indicating that the fluid flow in this region was significantly influenced by the rotation of the blades. This is consistent with the flow characteristics observed at the wall-monitoring points in the unsteady numerical calculations. (3) At measurement points M3 and M4, which were closer to the bottom of the runner chamber, the pressure pulsation primarily exhibited frequencies near the shaft frequency, suggesting that the fluid flow in this area was affected by the combined effects of gravity and blade rotation.

3. Structural Characteristics of the Runner Chamber under Fluid-Structure Interaction

This study utilized the ANSYS Workbench platform and integrated modules such as APDL, Fluent, and Static Structural for coupled simulations. Because the runner chamber structure is relatively stiff and resistant to deformation under the pressure of the flow field, its influence on the flow is negligible. Consequently, a one-way fluid-structure interaction (FSI) approach is adopted for the numerical calculations. The pressure on the runner chamber walls, obtained from Fluent's flow-field simulations, is applied to the inner surfaces of the structure at the fluid–structure interface. This allows the analysis of the structural response to the pressure exerted by the flow field, while the feedback from the structure on the fluid flow is disregarded.

3.1 Geometric Modeling and Theoretical Analysis of the Ring-Stiffened Structure

The runner chamber structure consists of a cavity and ring-stiffened reinforcement. The cavity is fabricated from 0Cr13Ni5Mo steel and is divided into upper and lower sections, which are fastened together with bolts. Ring-stiffened reinforcements are welded to the corners of the runner chamber cavity using Q235 steel plates. The material parameters are listed in Table 3.

In this study, to ensure the reliability and accuracy of the computational results and to eliminate the potential influence of mesh resolution, a detailed numerical model of the rotary chamber was established based on the structural design parameters. Nine different mesh discretization schemes were designed (as shown in Fig. 10 (a)). By comparing the first six modal frequencies and the average structural amplitude for each scheme, we were

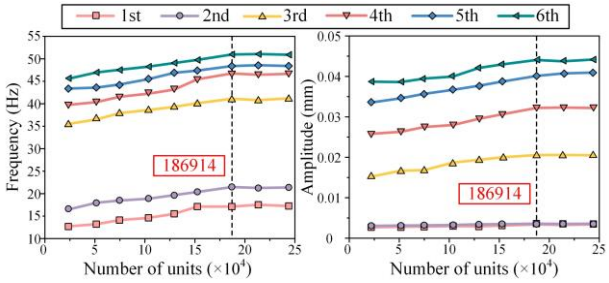

(a) The effect of grid resolution on the calculation results

Paramate	Data/mm	Paramate	Data/mm	Paramate	Data/mm	Paramate	Data/mm
R_1	3652	R_2	1113	R_3	3600	R_4	1486
R_5	3622	D_1	37	D_2	125	D_3	50

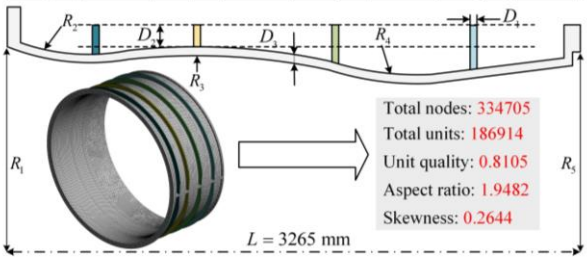

(b) Design parameters and grid display of runner chamber

Fig. 10 Verification of grid independence and grid display of runner chamber structure

able to assess the trade-off between computational accuracy and resource consumption. After careful consideration of these factors, a mesh configuration consisting of 186,914 elements was selected for the subsequent fluid-structure interaction (FSI) analysis, as it provided a good balance between precision and computational efficiency.

Figure 10 (b) provides a detailed overview of the structural design parameters and mesh characteristics for the selected scheme. The finite element mesh associated with this configuration has a unit quality of 0.8105, an aspect ratio of 1.9482, and a skewness of 0.2644. These values indicate that the mesh satisfies the necessary criteria for FSI calculations, ensuring sufficient accuracy while keeping computational resource consumption within an acceptable range. This selection enables reliable and efficient simulation of the coupled fluid-structure interaction, which is crucial for the integrity and performance evaluation of the rotary chamber.

Flügge's shell theory is a classical theory used to analyze thin-shell structures. Within this theoretical framework, the strain energy density of the shell can be expressed using the strain and stress tensors, as shown in Eqs. (3).

$$u_s = \frac{1}{2}\varepsilon : \sigma \tag{3}$$

In the equation, u_s represents the strain energy density, ε represents the strain tensor, σ represents the stress tensor, and ":" denotes the double-dot product (i.e., the inner product of the tensors). The stress and strain tensors can be decomposed into cylindrical coordinates, as follows:

$$\sigma=\begin{pmatrix}\sigma_x & \tau_{x\theta} & \tau_{xr}\\ \tau_{\theta x} & \sigma_\theta & \tau_{\theta z}\\ \tau_{rx} & \tau_{r\theta} & \sigma_r\end{pmatrix},\ \varepsilon=\begin{pmatrix}\varepsilon_x & \gamma_{x\theta} & \gamma_{xr}\\ \gamma_{\theta x} & \varepsilon_\theta & \gamma_{\theta z}\\ \gamma_{rx} & \gamma_{r\theta} & \varepsilon_r\end{pmatrix} \tag{4}$$

where σ_x represents the axial stress, σ_θ represents the circumferential stress, and σ_r represents the radial stress. Here, τ_{ij} denotes the shear stress acting on the j plane in the i direction. Similarly, ε_x, ε_θ, and ε_r represent the axial, circumferential, and radial strains, respectively. γ_{ij} denotes the shear strain in the j plane in the i direction. The stress and strain tensors can be expressed by Eqs. (5) and Eq. (6) (Qu & Meng, 2014).

$$\sigma_x=\frac{E}{1-\nu^2}\left(\varepsilon_x+\nu\varepsilon_\theta\right),\ \sigma_\theta=\frac{E}{1-\nu^2}\left(\varepsilon_\theta+\nu\varepsilon_x\right),\ \sigma_r=\frac{E}{2(1+\nu)}\varepsilon_r \tag{5}$$

$$\varepsilon_x=\frac{\partial u}{\partial x}-r\frac{\partial^2 w}{\partial x^2},$$

$$\varepsilon_\theta=\frac{\partial v}{R\partial x}-\frac{w}{R-r}-\frac{rR}{R-r}\frac{\partial^2 w}{\partial\theta^2},$$

$$\varepsilon_r=\frac{R}{R-r}\frac{\partial u}{R\partial\theta}+\frac{R-r}{R}\frac{\partial v}{\partial x}-\left(r+\frac{rR}{R-r}\right)\frac{\partial^2 w}{R\partial x\partial\theta} \tag{6}$$

where E represents the Young's modulus, ν is Poisson's ratio, and u,v,w are the displacements in the axial, circumferential, and radial directions, respectively. The strain energy U_s represents the energy stored in the material during deformation. For a given shell structure, the total strain energy can be obtained by integrating the strain energy density u_s over the entire volume V of the structure, as expressed in Eq. (7) (Zhou, 2012)

$$U_s=\int_V u_s dV=\int_V\frac{1}{2}\varepsilon_{ij}:\sigma_{ij}dV \tag{7}$$

The Hamilton principle provides a systematic energy-based approach for solving the equations of motion for complex structures. Based on the Hamilton principle, the framework of the equations of motion of the shell can be derived as shown in Eq. (8):

$$\delta\int_{t_1}^{t_2}\left(T_s+W-U_s\right)dt=0 \tag{8}$$

where δ represents the variation operation, T_s is the kinetic energy of the shell, including the contribution from the ring-stiffened ribs, W represents the work done by the fluid–solid interaction forces, and U_s represents the strain energy. This equation describes the balance between the kinetic energy, work, and strain energy of the system over a given time interval (t_1 to t_2). For thin shells, the displacement components $u,v,$ and w represent the shell displacements in the axial, circumferential, and radial directions, respectively. These displacements are described using modal expansion, where each mode represents a displacement pattern at a specific frequency, as shown in Eq. (9). In the equation, m and n denote the longitudinal and circumferential half-wave numbers, $f_{mn}{}^u(x,y,z)$, $f_{mn}{}^v(x,y,z)$, and $f_{mn}{}^w(x,y,z)$ are the spatial functions corresponding to each mode, and $U_{mn}(t)$, $V_{mn}(t)$, and $W_{mn}(t)$ are the time-dependent modal coefficients (Hemmatnezhad et al., 2015).

$$\begin{cases}u(x,r,\theta,t)=\sum_{m,n}U_{mn}(t)\,f_{mn}{}^u(x,y,z)\\ v(x,r,\theta,t)=\sum_{m,n}V_{mn}(t)\,f_{mn}{}^v(x,y,z)\\ w(x,r,\theta,t)=\sum_{m,n}W_{mn}(t)\,f_{mn}{}^w(x,y,z)\end{cases} \tag{9}$$

The kinetic energy of the shell T_s and the work done by the fluid-solid interaction forces W can be expressed as shown in Eqs. (10). In this equation, ρ represents the density of the shell material, $\dot{u}$, $\dot{v}$ and $\dot{w}$ are the time derivatives of the shell displacement components representing the velocity components, and dV is the differential volume element. F represents the forces exerted by the fluid on the shell surface, including both pressure and shear forces. $U=[u,v,w]^T$ represents the displacement of the shell in the axial, circumferential, and radial directions and $d\Omega$ is the differential surface area element.

$$T_s=\frac{1}{2}\int_V\rho\left(\dot{u}^2+\dot{v}^2+\dot{w}^2\right)dV,\ W=\int_\Omega F\cdot U d\Omega \tag{10}$$

Based on the aforementioned equations, the motion equation for the ring-stiffened cylindrical shell under hydraulic impact can be derived, as shown in Eq. (11). In this equation, ρ is the density of the shell material, h represents the effective thickness of the stiffened shell, and $\ddot{U}_{mn}(t)$, $\ddot{V}_{mn}(t)$, $\ddot{W}_{mn}(t)$ are the second-order time derivatives representing the accelerations of each mode in different directions. $\dot{W}_{mn}(t)$ is the first-order time derivative of the radial displacement component, representing the radial velocity of each mode. F_{mn} denotes the added mass from the fluid flowing over the cylindrical shell, reflecting the influence of fluid motion on the shell. U_f is the fluid flow velocity, and L_{ij} represents the stiffness matrix of the structure. Since the fluid flows in the axial direction, the damping effect of the fluid flowing over the shell must be considered, hence introducing the damping term $\frac{8F_{mn}mU_f}{L}\sum_{i=1}^{M}\frac{i}{m^2-i^2}W_{mn}(t)$, which accounts for the fluid's damping effect on the radial vibration of the shell (Zhou, 2012).

$$\begin{pmatrix} \rho h \ddot{U}_{mn}(t) \\ \rho h \ddot{V}_{mn}(t) \\ (\rho h + F_{mn}) \ddot{W}_{mn}(t) \end{pmatrix} + \begin{pmatrix} 0 \\ 0 \\ \dfrac{8F_{mn} m U_f}{L} \displaystyle\sum_{i=1}^{M} \dfrac{i}{m^2 - i^2} \dot{W}_{mn}(t) \end{pmatrix}$$

$$+ \begin{pmatrix} L_{11} & L_{12} & L_{13} \\ L_{21} & L_{22} & L_{23} \\ L_{31} & L_{32} & L_{33} \end{pmatrix} \begin{pmatrix} U_{mn}(t) \\ V_{mn}(t) \\ W_{mn}(t) \end{pmatrix} = 0 \qquad (11)$$

To transform the motion equation into a form suitable for finite element analysis, the inertia terms in the equation are extracted to form the mass matrix M, which is then extracted to form the damping matrix C, The displacement-related terms were extracted to form the stiffness matrix K. The modified equation of motion can then be expressed using Eq. (12).

$$M \begin{pmatrix} \ddot{U}_{mn}(t) \\ \ddot{V}_{mn}(t) \\ \ddot{W}_{mn}(t) \end{pmatrix} + C \begin{pmatrix} \dot{U}_{mn}(t) \\ \dot{V}_{mn}(t) \\ \dot{W}_{mn}(t) \end{pmatrix} + K \begin{pmatrix} U_{mn}(t) \\ V_{mn}(t) \\ W_{mn}(t) \end{pmatrix} = 0 \qquad (12)$$

The motion equation must be converted into an eigenvalue problem to obtain the natural frequencies and mode shapes of the system. Assuming that the solution takes the form of a simple harmonic function as shown in Eq. (13), where ω is the natural frequency of the system. Substituting this into the motion equation results in the form shown in Eq. (14).

$$\begin{pmatrix} U_{mn}(t) \\ V_{mn}(t) \\ W_{mn}(t) \end{pmatrix} = \begin{pmatrix} U_{mn} \\ V_{mn} \\ W_{mn} \end{pmatrix} e^{i\omega t} \qquad (13)$$

$$\left(-\omega^2 M + i\omega C + K\right) \begin{pmatrix} U_{mn} \\ V_{mn} \\ W_{mn} \end{pmatrix} = \begin{pmatrix} 0 \\ 0 \\ 0 \end{pmatrix} \qquad (14)$$

3.2 Modal Characteristics Analysis of the Turbine Runner Chamber

Based on an analysis of the ring-stiffened structure theory, finite-element numerical calculations of the pre-stressed and wet modes of the runner chamber structure were conducted. The results of the modal frequencies and shapes are shown in Fig. 11. Under the action of fluid pressure, the frequency range of the prestressed modes for the runner chamber varies from 113.75 Hz for the first mode to 204.6 Hz for the twentieth mode. In contrast, the frequency range for the wet mode spans from 51.50 Hz for the first mode to 98.06 Hz for the twentieth mode. The wet-mode frequencies are significantly lower than the prestressed mode frequencies, with no overlap in their frequency ranges, and the average decrease in the wet-mode frequency compared with the prestressed mode frequency is 53.36%. This reduction is attributed to the added mass effect of water when the runner chamber is submerged, which enhances the damping effect on the structure and alters its dynamic characteristics, thereby decreasing the natural frequency. Studies have shown a negative correlation between the density of a liquid and the natural frequency of a structure. Therefore, it is crucial

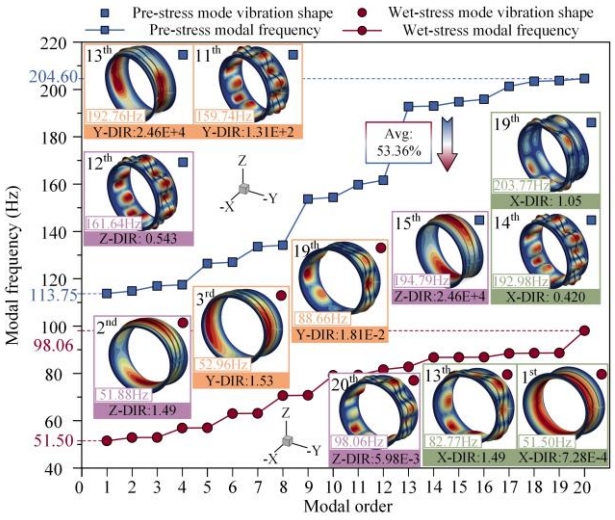

Fig. 11 Comparison of pre-stressed modes and wet modes in runner chamber

to consider the operating environment (e.g., water with sediment vs. clean water and fresh water vs. saline water) during the design of a turbine structure to avoid the expansion of the resonance frequency ranges.

During operation of the unit, water flows axially in the X-direction, causing greater deformation in the Y- and Z-directions than in the X-direction. By comparing the maximum effective masses in each direction, the maximum modal effective mass in the Y-direction was found to have significantly exceeded those in the X- and Z-directions, indicating a more pronounced response of the runner chamber in the Y-direction. Among the prestressed modes, the eleventh and thirteenth modes in the Y-direction warrant particular attention, whereas the twelfth and fifteenth modes in the Z-direction should also be closely monitored. In the wet modes, the maximum effective masses in the Y- and Z- directions remained greater than those in the X-direction, with special focus on the third and nineteenth modes in the Y-direction, and the second and twentieth modes in the Z-direction.

In addition, the figure shows the sixth order vibration modes with the highest modal effective mass in various directions for both modes. Given that the front and rear sides of the runner chamber are fixed by bolts, vibrations predominantly occurred along the Y- and Z-axes. From the vibration patterns, it can be observed that the vibrations of the runner chamber can be categorized into bending, twisting, and composite vibrations. In the prestressed modes, the thirteenth and fifteenth modes exhibited the maximum modal effective masses in the Y- and Z-directions, with the highest deformation occurring on the symmetrical sides of the structure along these axes. In contrast, the eleventh, twelfth, fourteenth, and nineteenth modes demonstrate a relatively low effective mass, with the deformation exhibiting a staggered fluctuation pattern around the circumference of the runner chamber, and the deformation of the outer stiffening ribs was complex. It is recommended that the structural parameters of the stiffening ribs be adjusted in the optimization design to enhance the vibration resistance.

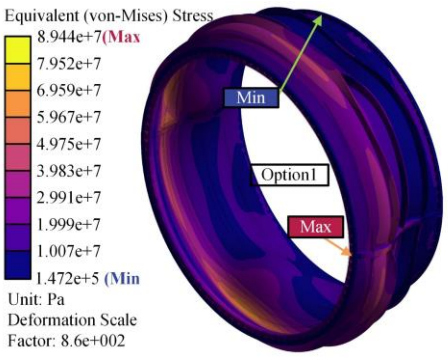

(a1) Equivalent stress in prestressed mode

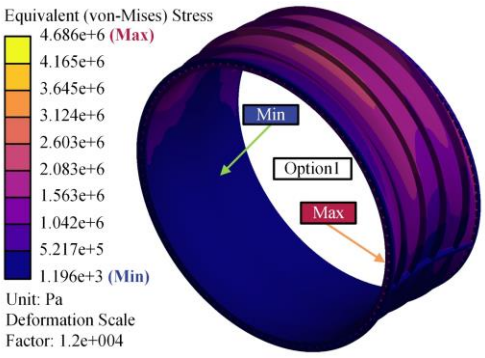

(a2) Equivalent stress in wet mode

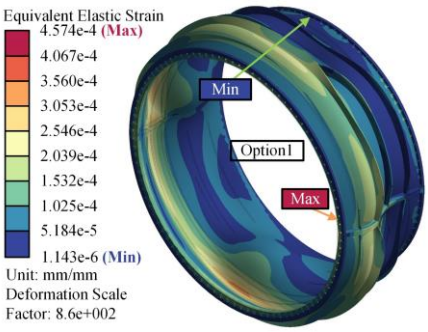

(b1) Equivalent elastic strain in prestressed mode

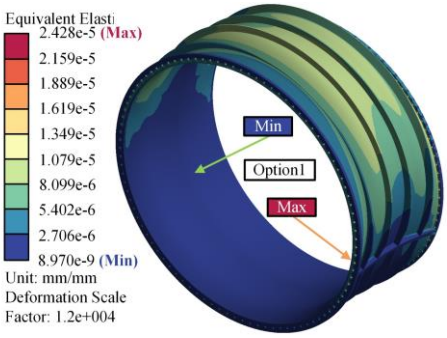

(b2) Equivalent elastic strain in wet mode

Fig. 12 Comparison of equivalent force and equivalent strain

In wet modes, the structural deformation significantly decreases owing to the added mass effect of the fluid. The second and third modes display maximum deformation that is uniformly distributed around the circumference, with the deformation directions interlacing internally and externally. The first mode shows a uniform distribution around the circumference, with the maximum deformation occurring at the radial midplane, gradually decreasing axially, and exhibiting minimum deformation at the bolt fastening points. The thirteenth, nineteenth, and twentieth modes exhibit the largest deformation components in the Z- and Y-directions and play a major role in the circumferential symmetry. Owing to the constraints imposed by the bolts in the X-direction, the dynamic response of all the modes in the X-direction is minimal, resulting in no significant displacement.

The stress and strain calculations for the structure under both modal conditions are shown in Fig. 12. In the prestressed mode, the equivalent stress (Fig. 12(a1)) ranges from 1.472e+5 Pa to 8.944e+7 Pa. The maximum stress occurs at the upstream bolt location, with a noticeable stress concentration in the shell area corresponding to the runner. This indicates that the hydraulic impact during runner rotation exerts significant stress in this region, highlighting the need to pay close attention to the structural strength and stability of this area. In the wet mode, the equivalent stress (Fig. 12(a2)) ranges from 1.196e+3 Pa to 4.686e+6 Pa, which represents a reduction of two orders of magnitude compared with the prestressed mode. This suggests that the pressure within the flow field has a more substantial effect on the wall of the runner chamber than on the gravitational pressure of the fluid. Additionally, the equivalent stress exhibits a symmetrical distribution across the circumferential section.

In prestressed mode, the maximum equivalent elastic strain (Fig. 12(b1)) is 4.574e-4 mm/mm, concentrated at the rivet fixation point on the upstream side. The strain concentration area appears on the inner wall, upstream, measuring 3.102e-4 mm/mm, indicating that the fluid exerts significant tensile loads on this region, resulting in considerable deformation. Considering the impact of the fluid mass and density on the structure, as shown in Fig. 12(b2), the maximum equivalent elastic strain in the wet mode is 2.428e-5 mm/mm and is concentrated at the rivet fixation point on the downstream side. The strain concentration area on the downstream wall measures 1.046e-5 mm/mm, suggesting a trend where the fluid causes the wall to bear greater tensile loads. To reduce the strain, optimization of the design of the stiffening ribs should be considered.

4. IMPROVEMENT OF THE STRUCTURAL PARAMETERS OF THE TURBINE RUNNER CHAMBER

4.1 Experimental Design and Optimal Scheme Establishment

Finite-element numerical simulation techniques are widely used in structural design research owing to their efficiency and accuracy. However, obtaining precise computational results requires significant computational resources. Therefore, the development of surrogate modeling methods (Kudela & Matousek, 2022) has emerged as an effective approach to address this challenge. This method typically treats the simulation software as a black box, constructs a surrogate model by collecting sample data, and allows the computational results to closely approximate the actual structural

analysis results while significantly reducing the required computational load.

In this study, the Latin Hypercube Sampling method is employed to design the experimental scheme, and optimization algorithms are combined to determine the optimal fit between the rib parameters, reinforcement forms, and structural responses, serving as the optimal structure for the runner chamber to ensure the stable and reliable operation of the turbine. In the analysis of the original runner chamber structure, the maximum stress occurs at the bolt fastening points; however, this location is not prone to inelastic deformation. By contrast, the wall area corresponding to the impeller position is identified as a frequent failure zone, exhibiting a significant stress concentration. To investigate the stress patterns in the wall area corresponding to the impeller position under different design schemes, monitoring points are set along the circumference to observe stress variations at different locations. The variables are defined based on the monitoring data from various positions and serve as evaluation criteria, as shown in Eq. (15).

$$\hat{y} = k_1 u_1 + k_2 u_2 + k_3 u_3 + k_4 u_4 \tag{15}$$

In the equation, u_1, u_2, u_3, u_4 represent the equivalent stresses (MPa) at different circumferential positions of the shell structure under hydraulic loading, while k_1, k_2, k_3, k_4 are the weighting coefficients for the equivalent stresses at these different positions. The shell design parameters D_1, D_2, D_3 are used as input variables for the experimental scheme, where D_1 represents the thickness of the rib plate, D_2 represents the height of the rib plate, and D_3 represents the thickness of the rib plate. The variable $\hat{y}$ serves as the output variable for the design scheme, assessing the feasibility of the design scheme. A total of 50 experiments were conducted, and the design schemes and calculation results are presented in the following table.

To ensure that the regression equation accurately describes the constructed relationships, it is necessary to validate the regression model. We employed the correlation coefficient method to test the significance of the regression equation. The standard deviation $Std\ Dev$, coefficient of determination R^2, adjusted coefficient of determination ${R_{adj}}^2$, and predicted coefficient of determination $pred.R^2$ are introduced for this validation.

$$Std\ Dev = \sqrt{\frac{1}{n}\sum_{i=1}^{n}(x_i - \bar{x})^2} \tag{16}$$

$$R^2 = \frac{{S_R}^2}{{S_T}^2} = 1 - \frac{{S_E}^2}{{S_T}^2} \tag{17}$$

$${R_{adj}}^2 = 1 - \frac{S_E/(n-m-1)}{S_T/(n-1)} = 1 - \frac{n-1}{n-m-1}(1-R^2) \tag{18}$$

$$pred.R^2 = 1 - \frac{S_E}{S_T + S_R} \tag{19}$$

Table 4 Experimental design program

Number	D_1 (mm)	D_2 (mm)	D_3 (mm)	$\hat{y}$
1	35.62	112.26	48.27	50.127
2	35.52	137.11	51.37	45.268
3	35.94	139.76	49.06	46.433
4	39.31	146.87	49.75	46.185
5	37.53	123.77	47.27	48.855
…	…	…	…	…
…	…	…	…	…
46	36.99	105.79	50.72	47.689
47	34.55	132.17	51.96	45.804
48	34.63	143.32	52.06	44.989
49	34.87	128.75	48.63	48.798
50	37.92	142.52	48.72	46.635

Table 5 Regression model reliability analysis

Type	$Std\ Dev$	R^2	${R_{adj}}^2$	$pred.R^2$
Primary polynomial	0.4082	0.8974	0.8940	0.8875
Quadratic polynomial	0.3759	0.9612	0.9525	0.9392
Cubic polynomial	0.3563	0.8339	0.8273	0.8186
Optimal range	≤10	≥0.9	${R^2}_{adj} - pred.R^2$ <0.2	

In the equations, x_i represents the value of the i data point, $\bar{x}$ is the mean of the dataset, $S_T$is the total sum of squares, $S_R$is the regression sum of squares, $S_E$is the sum of the squares of the residuals (the squared differences between the observed and predicted values), n is the sample size, and m is the number of optimization variables. it can be seen that when using a second-order model for regression analysis, the correlation coefficients are all greater than 90%, and the difference between and is within 0.2. This indicates that the second-order regression equation can be used to predict the relationship between the structural parameters of the turbine runner chamber and response, as shown in Eq. (20).

Table 5 presents the reliability and error analyses of the different polynomial models. Based onit can be seen that when using a second-order model for regression analysis, the correlation coefficients are all greater than 90%, and the difference between and is within 0.2. This indicates that the second-order regression equation can be used to predict the relationship between the structural parameters of the turbine runner chamber and response, as shown in Eq. (20).

$$\begin{aligned}\hat{y} = &-3.80163D_1 - 0.306512D_2 - 3.69353D_3 \\ &+0.004029D_1D_2 + 0.032284D_1D_3 \\ &+0.004010D_2D_3 + 254.21616\end{aligned} \tag{20}$$

In this equation, $\hat{y}$ represents the model response, measured in MPa; D_1, D_2, and D_3 represent the width of the rib, height of the rib, and wall thickness of the shell, respectively, all measured in millimeters. Based on the

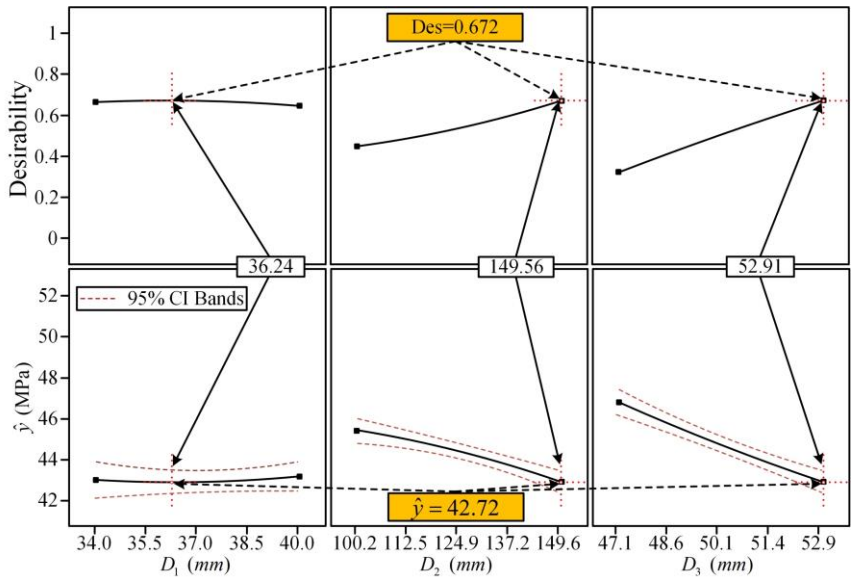

Fig. 13 Schematic representation of the optimal design solution

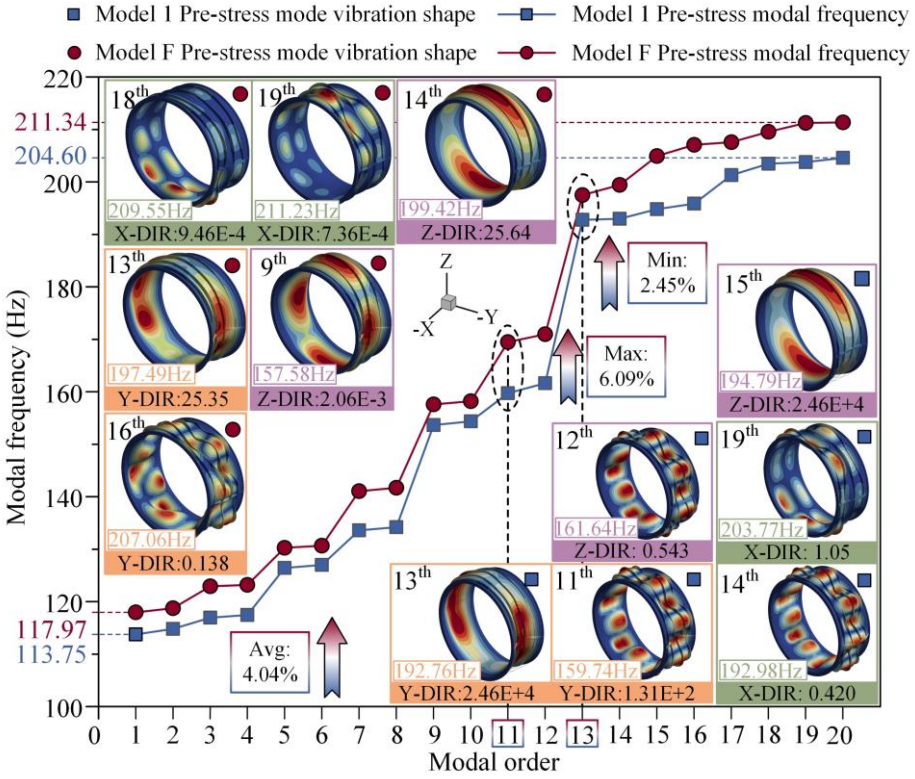

Fig. 14 Comparison of prestressed modes of optimized and original structures.

Table 6 Projected program feasibility analysis

Test number	D_1 (*mm*)	D_2 (*mm*)	D_3 (*mm*)	Actual $\hat{y}$	Expected $\hat{y}$	Error %
1	36.24	149.56	52.19	43.31	42.72	1.38
2	36.24	149.56	52.19	42.45	42.72	0.63
3	36.24	149.56	52.19	41.87	42.72	1.98

data calculated from the experimental design, optimal predictions for the design scheme were made using optimization algorithms, as illustrated in Fig. 13.

When the structural parameters were set to: D_1 = 36.24 mm, D_2 = 149.56 mm, and D_3 = 52.19 mm, the response of the shell reached a minimum value of 42.72

MPa, with a desirability/satisfaction level of 0.672. A feasibility analysis of the predicted results is presented in Table 6. To eliminate the influence of the finite element software on the results, three numerical calculations were performed for the optimal design scheme, revealing a maximum error of 1.98%, which is less than 5%. This demonstrates the reliability of the optimization algorithm for predicting the relationship between the structural response and the structural parameters.

4.2 Comparison and Analysis of Optimization Schemes

The optimal structure is defined as Model F, and the initial structure is defined as Model 1. Fig. 14 illustrates a comparison of the prestressed modal characteristics of the two models. It is evident that the modal frequencies of Model F are generally higher than those of Model 1, particularly in the 11th mode, where the frequency increases significantly by 6.09%. The 13th mode shows the least change, with a 2.45% increase. Notably, Model F also exhibits considerable improvements in the lower modes, with the frequencies of the 3rd and 4th modes increasing by 5.11% and 4.86%, respectively. These results indicate that the overall stiffness of the optimized structure Model F is significantly enhanced compared with that of Model 1.

The modal effective mass is a critical parameter for assessing the intensity of the vibrational response of a structure in specific directions. Analysis of the maximum modal effective mass of both models reveals that the effective masses in the Y- and Z-directions exceed that in the X- direction. This is primarily because, during operation, the water flow moves axially (in the X-direction), resulting in a smaller vibration response in this direction. Comparing the maximum effective mass in each direction, Model F shows a lower modal effective mass than Model 1, particularly in the Y-direction, where the maximum effective mass values of Model 1 are 1.31E+2 and 2.46E+4, whereas those of the optimized structure drop to 0.138 and 25.35, respectively. This indicates that the optimized structure exhibits a significant improvement in the Y-direction vibration response, and similar conclusions apply to the analysis of the Z-direction modal effective mass.

Furthermore, the figure shows the modal shape distributions for Models 1 and F under various modes. In Model 1, certain high-order modes (such as the 12th and 14th) show concentrated vibration patterns in specific areas, indicating notable vibration concentration phenomena. In contrast, Model F demonstrates more uniform vibration patterns across multiple modes, leading to a significant optimization of the vibration response. This suggests that the optimized shell structure distributes the vibrational energy more evenly when subjected to external impacts, thereby enhancing the stability and durability of the structure and significantly improving its overall performance under complex operating conditions.

Figure 15 presents a comparison of the two models under wet modal conditions. Overall, Model F exhibits higher frequencies across all modal orders than Model 1, indicating that the optimized Model F possesses greater stiffness and enhanced vibration resistance under hydrostatic pressure. Specifically, the frequency increase is the most pronounced in the 16th mode, which increases by 77.78%, whereas the 8th mode shows the least change, with an increase of 44.39%. The average frequency increase for the first 20 modes is 58.45%, further validating the significant enhancement in the structural stiffness of Model F under hydrostatic pressure compared to Model 1.

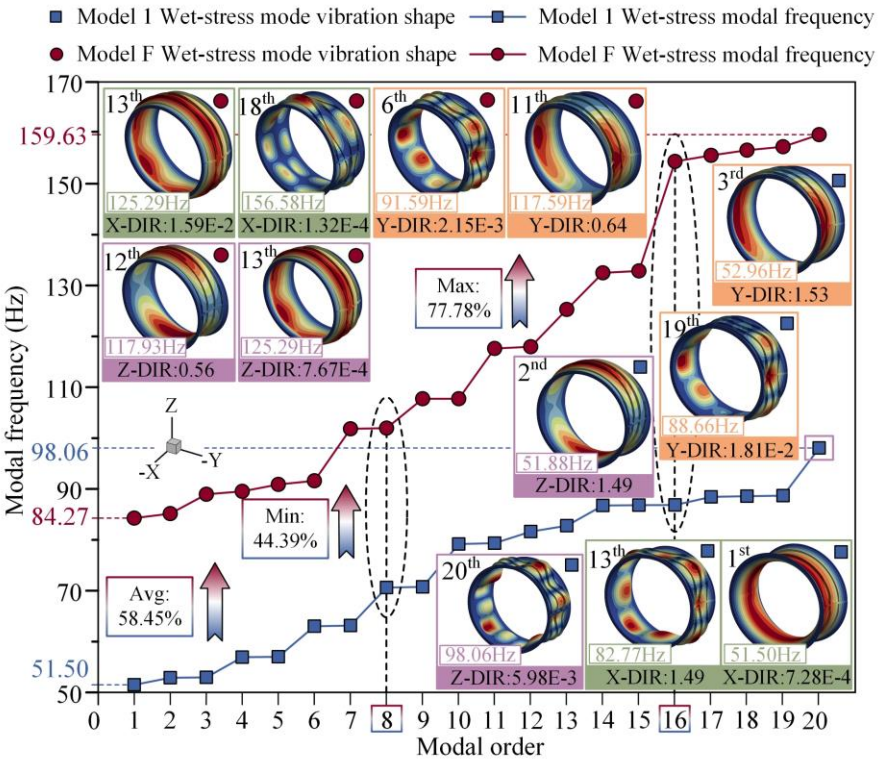

Fig. 13 Comparison of wet modal state between optimized and original structure

The modal effective mass analysis indicates that both structures exhibit a greater modal effective mass in the Y- and Z-directions than in the X-direction. This is primarily because the hydrostatic pressure acts mainly in the radial and axial directions with a comparatively smaller effect in the axial (X) direction. A further comparison reveals that the maximum modal effective mass of Model F is lower than that of Model 1, signifying a significant optimization in the vibration response of Model F, particularly enhancing the stability of the structure in critical directions.

The mode shape diagrams illustrate the distribution of the structural deformation under different modes. In the first three modes of Model 1, the mode shapes display a notable localized vibration concentration, which was particularly pronounced in the middle of the shell. In contrast, the mode shapes of Model F are more uniform, with a significant reduction in the overall and localized deformation areas. This indicates that, under hydrostatic pressure, the optimized structure allows for a more rational distribution of vibrational energy, thereby enhancing the overall structural stability of Model F. In summary, the optimized Model F demonstrates clear advantages in the modal frequency distribution and vibration control capabilities. Under wet modal conditions, the structural stiffness and vibration resistance characteristics of Model F are comprehensively improved, exhibiting stronger stability and superior vibration performance.

Figure 16 shows the equivalent stress distribution cloud diagrams for both models under the same hydraulic impact and constraints. Figure 16 (a), (b), (c), and (d) respectively present top, bottom, left, and right views of the casing. The red boxes highlight the stress concentration areas that correspond to the impeller-facing section of the turbine chamber walls and serve as the primary focus for analysis and optimization. The numerical results indicated that the maximum stress occurs at the bolt junction of the upstream side and extended along the axial direction. However, because of the bolted connection, axial strain in the casing is not significant; therefore, the stress distribution in the bolted region is excluded from the analysis. In Model 1, the maximum stress in all four views appears on the right side of the casing and is measured at 48.19 MPa. In contrast, optimized Model F shows a reduced maximum stress of 43.36 MPa on the right side, which is a reduction of 11.1%. In addition to the right side, a comparison of the maximum stresses on the top, bottom, and left sides reveals that the optimized Model F has lower stresses than Model 1, with reductions of 4.57%, 4.31%, and 4.35%, respectively. This demonstrates that the optimized structure provides a more favorable stress distribution at the peak stress points.

In conclusion, compared to Model 1, the optimized Model F not only exhibits a more uniform stress distribution, but also significantly reduces stress concentrations in critical regions. These improvements enhance the fatigue resistance of the structures. In addition, the stiffening rib design in Model F effectively increases the stiffness of the casing and improves the

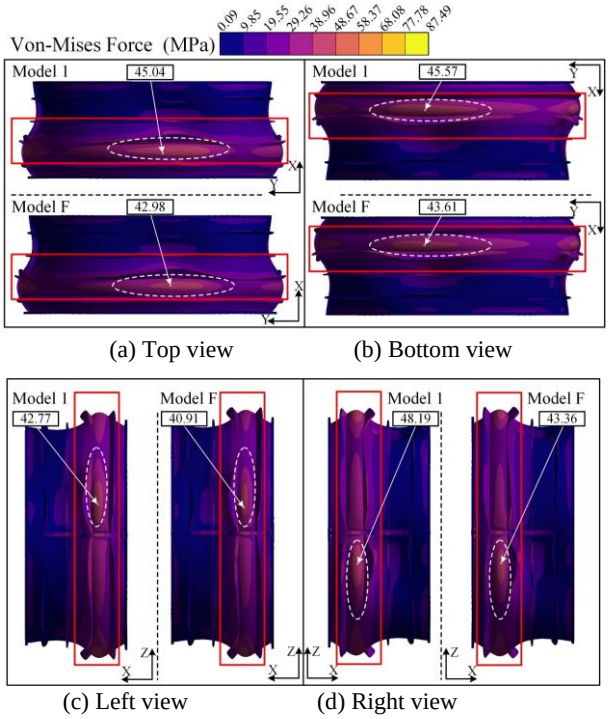

Fig. 14 Stress distribution in two structures under hydrodynamic impact

stress distribution across all viewpoints. These enhancements enable the optimized design to have greater reliability under real-world operating conditions, allowing it to withstand more complex hydraulic impacts, showcasing superior performance and longer service life.

The distribution of equivalent elastic strain in both models closely resembles the stress distribution. Figure 17 shows the equivalent elastic strain distribution cloud diagrams for both models under the same hydraulic impact and constraints, with Fig. 17 (a), (b), (c), and (d) representing the top, bottom, left, and right views of the casing, respectively. The red boxes indicate the strain concentration regions. In Model 1, the maximum strains on the top and bottom sides are 2.17e-4 mm/mm and 2.18e-4 mm/mm, respectively. In contrast, the optimized Model F shows maximum strains of 2.04e-4 mm/mm and 2.07e-4 mm/mm, reflecting reductions of 5.99% and 5.05%, respectively. A comparison of the maximum strain values on the left and right sides also reveals improvements in optimized Model F, with reductions of 5.71% and 7.01%, respectively. This indicates that the optimized model performs better in the regions of maximum strain.

Beyond the areas of maximum strain, the optimization effect is more evident in reducing the overall strain distribution within the strain concentration zones. The area of the strain concentration was significantly reduced in Model F, as indicated by the dashed boxes in the figure. This improvement suggests that the optimized model has better structural deformation uniformity when subjected to loads, thereby decreasing the risk of excessively high local strain. Consequently, the overall performance and durability of the structure are enhanced.

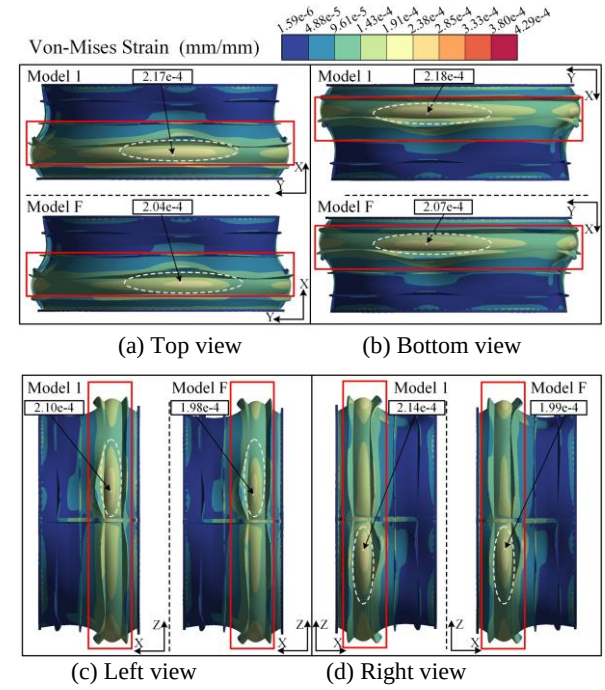

Fig. 15 Strain distribution in two structures under hydrodynamic impact

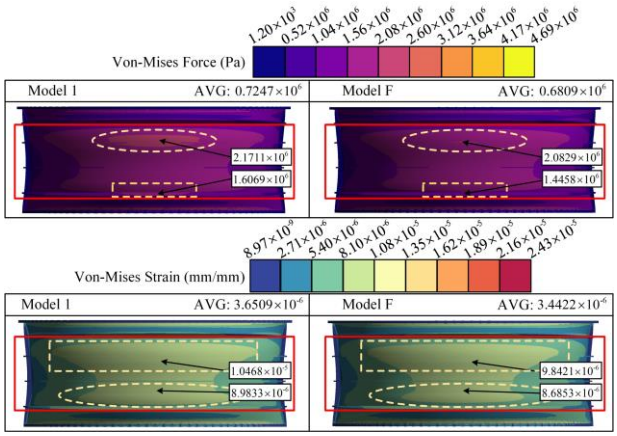

Fig. 16 Stress and strain distribution in two structures under hydrostatic pressure

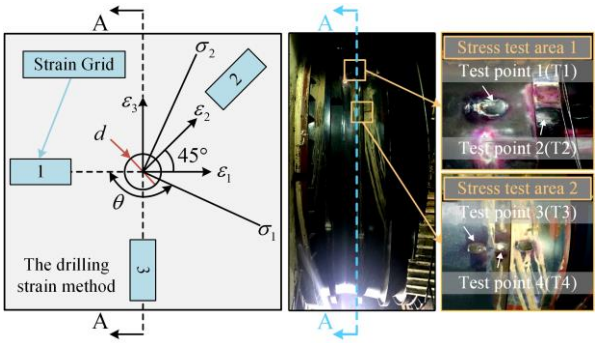

Fig. 17 Stress test principle and installation position

Additionally, we examined the responses of the two structures under static water pressure conditions. By comparing the stress and strain distributions of the unoptimized Model 1 and optimized Model F under these conditions, we can understand the improvements brought about by the optimization under actual operating conditions more clearly. The Von Mises stress distribution cloud diagram reveals that Model 1 exhibits a significant stress concentration in the bottom region, particularly in the center of the bottom surface of the casing and along the edge areas. The maximum stress in Model 1 is 2.1711e+6 Pa. In contrast, although the stress concentration areas remain in optimized Model F, the maximum stress is reduced to 2.0829e+6 Pa, reflecting a 4.1% reduction. This indicates that the optimized structure demonstrates better compression resistance under wet modal conditions and can better handle the loads caused by static water pressure.

Similarly, the Von Mises strain distribution cloud diagram shows that the maximum strain at the bottom of Model 1 is 1.0468e−5 mm/mm, whereas the maximum strain in the optimized Model F is reduced to 9.8421e−6 mm/mm, representing a 6.3% decrease. This result further confirms the advantages of the optimized design for improving structural uniformity and reducing localized deformation. Overall, these findings demonstrate that the optimized Model F offers enhanced structural performance and durability under both hydraulic and static loading conditions, leading to improved reliability in real-world applications.

4.3 Experimental Validation

To verify the accuracy of the numerical calculations, this study conducted residual stress measurements at designated test points following the standards of "Field Test Procedures for Vibration and Pulsation of Hydraulic Machinery" (GB/T 17189-2017) and "Determination of Residual Stress in Metallic Materials - Hole Drilling Strain-Gauge Method" (GB/T 31310-2014). The measurements were performed using two types of testing equipment (as listed in Table 7). The locations of the test points are shown in Fig. 19.

In the shutdown state of the turbine unit, the hole-drilling strain gauge method was used to measure the residual stress on the outer surface of the turbine runner chamber. Four measurement points were set: T1 and T3 were located in the runner chamber, and T2 and T4 were positioned on the circumferential ribs of the runner chamber. Prior to measurements, the test locations were polished and ground to ensure smooth surfaces. Subsequently, TJ120 strain gauges were applied to the test points and connected to measurement instruments for the drilling procedure. A YC-III testing device was used to collect the three-directional strain data at each point, which were recorded for further analysis. Residual stress was calculated using the following equation:

Table 7 Stress test equipment

Name	Model	Measuring range	Measuring accuracy
Residual Stress Tester	YC-III	1με~100000με	±0.05%
Resistance Strain Gauge	TJ120	φ 1.5	Sensitivity factor：2.07±1%

Table 8 Stress test results

Test point	σ_1/MPa	σ_2/MPa	θ/°
T1	+65	-17	-35˚
T2	+281	+63	18˚
T3	-10	-85	10˚
T4	+294	+110	-23˚

$$\begin{cases} \sigma_1 = \dfrac{A}{4E}(\varepsilon_1+\varepsilon_2) - \dfrac{B}{4E}\sqrt{(\varepsilon_1-\varepsilon_3)^2+(2\varepsilon_2-\varepsilon_1-\varepsilon_3)^2} \\ \sigma_2 = \dfrac{A}{4E}(\varepsilon_1+\varepsilon_2) + \dfrac{B}{4E}\sqrt{(\varepsilon_1-\varepsilon_3)^2+(2\varepsilon_2-\varepsilon_1-\varepsilon_3)^2} \\ \tan(2\theta) = \dfrac{2\varepsilon_2-\varepsilon_1-\varepsilon_3}{\varepsilon_3-\varepsilon_1} \end{cases} \quad (21)$$

where ε_1, ε_2, and ε_3 represent the released strains in three directions; σ_1 and σ_2 are the maximum and minimum principal stresses, respectively; θ is the angle between the reference axis of strain gauge No. 1 and σ_1; E is the elastic modulus of the material; A and B are the two strain-release coefficients of the material.

Based on the experimental results (Table 8), the following conclusions can be drawn: (1) Significant tensile stress was observed on the circumferential ribs of the runner chamber, whereas the residual stress level within the chamber body itself was relatively low. (2) The maximum principal stress direction at all four measurement points was approximately parallel to the direction of the circumferential ribs and nearly perpendicular to the direction of crack propagation on the ribs. This indicates that the high residual stress on the circumferential ribs is a critical factor that contributes to the formation and propagation of cracks in the runner chamber. (3) A comparative analysis revealed that the tensile and compressive stress trends at all four measurement points were consistent. In addition, the numerical simulation results for the principal stresses were within the range of the experimentally measured maximum and minimum principal stresses. This consistency suggests that the modal finite element analysis of the structure is highly accurate and reliable.

5. CONCLUSION

This study investigated the pressure pulsation characteristics and flow-induced vibration behavior in the runner chamber of a bulb turbine under low-flow conditions by combining CFD simulations and experimental validation. The key findings are summarized as follows.

1. Pressure pulsations within the flow field exhibited distinct axial and radial distribution patterns. Sampling points near the axis were primarily influenced by the rotational frequency (1.14 Hz), whereas those near the blades were dominated by the blade-passing frequency (4.54 Hz). The pulsation amplitude decreased progressively from upstream to downstream and from the wall of the flow passage toward the central axis.
2. Modal analysis indicated that horizontal vibration dominated the structural deformation under the impact of the flow field. Due to the fluid-added mass effect, wet modal frequencies were reduced by 53.36% compared to prestressed modal frequencies, highlighting strong coupling between unsteady flow and structural dynamics. Stress concentration zones were directly correlated with local regions of high-amplitude pressure pulsations, confirming that flow-induced loading is the primary driver of structural fatigue.
3. Compared with the original structure, the optimized runner chamber design obtained through multi-parameter collaborative optimization exhibited increases of 4.04% and 58.45% in prestressed and wet modal frequencies, respectively. Under flow-induced hydraulic impacts, maximum stress and strain were reduced by 11.1% and 7.01%, respectively. These results demonstrate the effectiveness of fluid-driven structural optimization strategies.

ACKNOWLEDGEMENTS

The authors are thankful for the support of the National Natural Science Foundation of China (52269022, 52179086, U2004183, 52177063).

CONFLICT OF INTEREST

The authors have no conflicts to disclose.

AUTHORS CONTRIBUTION

Houbin Song: Conceptualization (equal); Writing review & editing. **Wenqi Xie:** Conceptualization (equal); Date curation (equal); Methodology (equal); Soft-ware (equal); Writing - original draft (equal); Writing - re-view. **Wei Han:** Supervision (equal); Validation (equal): Writing - review & editing (equal). **Hongbo Qiu:** Method-ology (supporting). **Zhijun Cuan:** Methodology (supporting). **Shuai Wang:** Methodology (supporting). Xiaolong Huang: Methodology (supporting).

REFERENCES

Ahn, S. H., Xiao, Y., Wang, Z., Zhou, X., & Luo, Y. (2017). Performance prediction of a prototype tidal power turbine by using a suitable numerical model. *Renewable Energy*, *113*, 293-302. https://doi.org/10.1016/j.renene.2017.06.021

Ahn, S. H., Zhou, X., He, L., Luo, Y., & Wang, Z. (2020). Numerical estimation of prototype hydraulic efficiency in a low head power station based on gross head conditions. *Renewable Energy*, *153*, 175-181. https://doi.org/10.1016/j.renene.2020.01.113

Amiri, K., Mulu, B., MJ, C., & Raisee, M. (2016). Effects of load variation on a Kaplan turbine runner. *International Journal of Fluid Machinery and Systems*, *9*(2), 182-193. https://doi.org/10.5293/IJFMS.2016.9.2.182

Bai, X., Tang, R., Zan, Y., & Li, J. (2019). Stability analysis of a cylindrical shell with axially symmetric defects under axial compression based on the reduction stiffness method. *Ocean Engineering*, *193*, 106584. https://doi.org/10.1016/j.oceaneng.2019.106584

Cao, J., Tian, H., Ahn, S. H., Duo, W., Bi, H., Zhao, L., Zhao, G., Gao, H., Wang, M., Ma, G., Wang, Z. & Liu, Y. (2022). Fatigue analysis in rotor of a prototype bulb turbine based on fluid-structure interaction. *Engineering Failure Analysis*, *132*, 105940. https://doi.org/10.1016/j.engfailanal.2021.105940

Cao, J., Yang, G., Luo, Y., Chen, J., Liao, R., & Wang, Z. (2022b). Failure investigation of a Kaplan turbine blade lever. *Engineering Failure Analysis*, *142*, 106840. https://doi.org/10.1016/j.engfailanal.2022.106840

Chen, K., Zhang, W., Xia, B., Tong, P., & Yang, L. (2024). Experimental and numerical study on the flow and heat transfer of ring-ribbed tank in deep-sea manned submersible. *Ocean Engineering*, *312*, 119091. https://doi.org/10.1016/j.oceaneng.2024.119091

Chen, M., Xie, K., Jia, W., & Xu, K. (2015). Free and forced vibration of ring-stiffened conical–cylindrical shells with arbitrary boundary conditions. *Ocean Engineering*, *108*, 241-256. https://doi.org/10.1016/j.oceaneng.2015.07.065

Esmaeilzadehazimi, M., Bakhtiari, M., Toorani, M., & Lakis, A. A. (2024). Numerical modeling and analysis of fluid-filled truncated conical shells with ring stiffeners. *Journal of Fluids and Structures*, *127*, 104121. https://doi.org/10.1016/j.jfluidstructs.2024.104121

Gao, C., Pang, F., Li, H., Huang, X., & Liang, R. (2024). Prediction of vibro-acoustic response of ring stiffened cylindrical shells by using a semi-analytical method. *Thin-Walled Structures*, *200*, 111930. https://doi.org/10.1016/j.tws.2024.111930

Georgievskaia, E. (2021). Analytical system for predicting cracks in hydraulic turbines. *Engineering Failure Analysis*, *127*, 105489. https://doi.org/10.1016/j.engfailanal.2021.105489

Moraga, G., Mut, V., Girardelo, J., Mazzouji, F., Valentin, D., Egusquiza, M., Egusquiza, E. & Presas, A. (2024). Excessive vibrations experienced in a Kaplan turbine at speed no load. *Engineering Failure Analysis*, *160*, 108228. https://doi.org/10.1016/j.engfailanal.2024.108228

Guo, Q., Zhou, L., & Wang, Z. (2015). Comparison of BEM-CFD and full rotor geometry simulations for the performance and flow field of a marine current turbine. *Renewable Energy*, *75*, 640-648. https://doi.org/10.1016/j.renene.2014.10.047

Hemmatnezhad, M., Rahimi, G. H., Tajik, M., & Pellicano, F. (2015). Experimental, numerical and analytical investigation of free vibrational behavior of GFRP-stiffened composite cylindrical shells. *Composite Structures*, *120*, 509-518. https://doi.org/10.1016/j.compstruct.2014.10.011

Jin, S., Li, Z., Gao, T., Huang, F., Gan, D., & Cheng, R. (2021). Constrained shell finite element method of modal buckling analysis for thin-walled members with curved cross-sections. *Engineering Structures*, *240*, 112281. https://doi.org/10.1016/j.engstruct.2021.112281

Kudela, J., & Matousek, R. (2022). Recent advances and applications of surrogate models for finite element method computations: a review. *Soft Computing*, *26*(24), 13709-13733. https://doi.org/10.1007/s00500-022-07362-8

Velasquez, L., Romero-Menco, F., Rubio-Clemente, A., Posada, A. & Chica, E. (2024). Numerical optimization and experimental validation of the runner of a gravitational water vortex hydraulic turbine with a spiral inlet channel and a conical basin. *Renewable Energy 220*, 119676. https://doi.org/10.1016/j.renene.2023.119676

Lee, H., & Kwak, M. K. (2015). Free vibration analysis of a circular cylindrical shell using the Rayleigh–Ritz method and comparison of different shell theories. *Journal of Sound and Vibration*, *353*, 344-377. https://doi.org/10.1016/j.jsv.2015.05.028

Li, T. S., Feng, J. J., Zhu, G. J., Li, Y. Z., & Luo, X. Q. (2023). Correlation analysis of cavitation-induced pressure pulsation and vibration in a bulb turbine. *Journal of Hydrodynamics*, *35*(6), 1052-1063. https://doi.org/10.1007/s42241-024-0084-9

Liu, Y., Zhu, R., Qin, Z., & Chu, F. (2022). A comprehensive study on vibration characteristics of corrugated cylindrical shells with arbitrary boundary conditions. *Engineering Structures*, *269*, 114818. https://doi.org/10.1016/j.engstruct.2022.114818

Qu, Y., & Meng, G. (2014). Three-dimensional elasticity solution for vibration analysis of functionally graded hollow and solid bodies of revolution. Part I: Theory. *European Journal of Mechanics-A/Solids*, *44*, 222-233. https://doi.org/10.1016/j.euromechsol.2013.11.004

Rahmatian, M. A., Nazarian Shahrbabaki, A., & Moeini, S. P. (2023). Single-objective optimization design of convergent-divergent ducts of ducted wind turbine using RSM and GA, to increase power coefficient of a small-scale horizontal axis wind turbine. *Energy 269*, 126822. https://doi.org/10.1016/j.energy.2023.126822

Roig, R., Sánchez-Botello, X., Escaler, X., Mulu, B., & Högström, C. M. (2022). On the rotating vortex rope and its induced structural response in a Kaplan turbine model. *Energies*, *15*(17), 6311. https://doi.org/10.3390/en15176311

Shan, C., Sun, J., Jia, X., Wu, R., & Lu, X. (2024). The mechanical behavior of cylindrical shell with composite corrugations under uniform and concentrated pressure. *Ocean Engineering*, *298*,

117148. https://doi.org/10.1016/j.oceaneng.2024.117148

Soltani Dehkharqani, A., Engström, F., Aidanpää, J. O., & Cervantes, M. J. (2019). Experimental investigation of a 10 MW prototype kaplan turbine during start-up operation. *Energies*, *12*(23), 4582. https://doi.org/10.3390/en12234582

Su, Z., Jin, G., & Ye, T. (2014). Three-dimensional vibration analysis of thick functionally graded conical, cylindrical shell and annular plate structures with arbitrary elastic restraints. *Composite Structures*, *118*, 432-447. https://doi.org/10.1016/j.compstruct.2014.07.049

Velásquez, L., Posada, A., & Chica, E. (2022). Optimization of the basin and inlet channel of a gravitational water vortex hydraulic turbine using the response surface methodology. *Renewable Energy 187*, 508-521. https://doi.org/10.1016/j.renene.2022.01.113

Wang, X., & Luo, S. (2010). *Vibration analysis of large bulb tubular pumping station considering flow-structure interaction*. 2010 Asia-Pacific Power and Energy Engineering Conference (pp. 1-4). IEEE. https://doi.org/10.1109/APPEEC.2010.5448926

Wang, Z., Chen, J., & Zhang, R. (2023). Calculation method for the interface contact stress of steel tube-to-sleeve grouted connections subjected to bending moments. *Structures*, *51*, 1095-1108). https://doi.org/10.1016/j.istruc.2023.03.111

Weili, L., Hongbo, Q., Xiaochen, Z., & Ran, Y. (2012). Influence of copper plating on electromagnetic and temperature fields in a high-speed permanent-magnet generator. *IEEE Transactions on Magnetics*, *48*(8), 2247-2253. https://doi.org/10.1109/TMAG.2012.2190740

Wu, Y., Li, C., Wang, X., & Zhu, G. (2021). *Study on the influence of tip clearance of tidal tubular turbine on pressure pulsation of draft tube.* IOP Conference Series: Earth and Environmental Science (Vol. 766, No. 1, p. 012026). IOP Publishing. https://doi.org/10.1088/1755-1315/766/1/012026

Yang, Y., Li, J. J., Zhang, Y., He, Q., & Dai, H. L. (2021). A semi-analytical analysis of strength and critical buckling behavior of underwater ring-stiffened cylindrical shells. *Engineering Structures*, *227*, 111396. https://doi.org/10.1016/j.engstruct.2020.111396

Zhang, M., Valentín, D., Valero, C., Egusquiza, M., & Egusquiza, E. (2019). Failure investigation of a Kaplan turbine blade. *Engineering Failure Analysis*, *97*, 690-700. https://doi.org/10.1016/j.engfailanal.2019.01.056

Zhao, Y., Li, Y., Feng, J., Dang, M., Ren, Y., & Luo, X. (2023). Vibration characteristics of a tubular turbine prototype at different heads with considering free surface and water gravity. *Water*, *15*(4), 791. https://doi.org/10.3390/w15040791

Zhou, X. (2012). Vibration and stability of ring-stiffened thin-walled cylindrical shells conveying fluid. *Acta Mechanica Solida Sinica*, *25*(2), 168-176. https://doi.org/10.1016/S0894-9166(12)60017-2